



Synthesis, characterization and application of graphene-based silver orthophosphate nanocomposite in organic dye degradation

Mehdi Al Kausor^{a,*}, Abdul Matin Ali^b, Susmita Sen Gupta^b, Dhruva Chakraborty^b

^aDepartment of Chemistry, Science College, Kokrajhar, Assam, India, Tel. +919706580448; email: mehdialkausar@gmail.com

^bDepartment of Chemistry, B.N. College, Dhubri, Assam, India, Tel. +917002739569; email: abdulmatinali@gmail.com (A.M. Ali), Tel. +919435561231; email: susmita2101@yahoo.co.in (S.S. Gupta), Tel. +91943028800; email: chakraborttydhruva@gmail.com (D. Chakrabortty)

Received 23 March 2018; Accepted 29 October 2018

ABSTRACT

The visible light driven semiconductor photocatalyst is a promising material in environmental pollution mediation. Silver orthophosphate has attracted considerable attention for its applications in this field. But the photocatalytic activity and stability is limited due to its photocorrosion during photocatalysis. In this work, a modified reduced graphene oxide (RGO) based silver orthophosphate heterostructure nanocomposite was synthesized by sol-gel and hydrothermal method. The nanocomposite was characterized by XRD, SEM, Raman, FTIR, diffuse reflectance spectra (DRS) and photoluminescence (PL) spectroscopy. The XRD and SEM indicated the formation of cubic silver orthophosphate nanoparticles deposited on RGO sheets. The FTIR and Raman spectra showed the interaction of silver orthophosphate nanoparticles with RGO. The DRS showed higher absorption of visible radiation and PL implied that these nanocomposites could effectively separate the photogenerated electron-hole pairs. The photocatalytic activity was tested in decolourization of Acid Blue 25, a toxic anthraquinonic dye in aqueous medium under visible light illumination. The kinetics of the degradation was studied by modified Langmuir–Hinshelwood mechanism. The result of this work revealed that heterostructure nanocomposite of silver orthophosphate grafted on reduced graphene oxide sheets could be easily synthesized by simple sol-gel and hydrothermal method and the photocatalytic activity of silver orthophosphate was greatly enhanced when integrated with RGO.

Keywords: Photocatalysis; Nanocomposite; Silver orthophosphate; Acid Blue 25; Heterostructure

1. Introduction

A wide variety of organic pollutants are introduced into the water system from various sources such as industrial effluents, agricultural runoff, and chemical spills [1]. Their toxicity, stability to natural decomposition, and persistence in the environment has been the cause of much concern to societies and regulatory authorities around the world [2]. Dye effluents from textile industries and photographic industries are becoming a serious environmental problem because of their toxicity, unacceptable colour, high chemical oxygen

demand content, and resistance to chemical, photochemical and biological degradation.

The treatment of environmental pollutants in waste water by active semiconductor photocatalysts has recently attracted considerable attention for its ability to completely oxidize organic contaminants to carbon dioxide, water and mineral acids [3–5]. Photocatalysis based on semiconductor is the most promising technology due to its potential applications in many aspects mainly in degradation of organic pollutants. [6,7]. Titanium dioxide (TiO₂) has been extensively studied as a photocatalyst for the degradation of pollutants and solar

* Corresponding author.

energy conversion [8]. However, due to its wide band gap and low quantum yield, it has some limitations in application. Silver orthophosphate has attracted considerable attention for its applications in this field [9,10]. But the photocatalytic activity and stability is limited due to its photocorrosion during photocatalysis. During the photocatalytic process, the transformation of Ag^+ into Ag usually takes place, which results in the photocorrosion of Ag_3PO_4 in the absence of electron acceptors [11]. The recombination of photogenerated electron–hole pairs, the redox potential of generated electron, and the surface status of Ag_3PO_4 are considered as factors that affect its photocatalytic performances. Further, along with the photocatalytic reaction, the appearance of by-product, black metallic Ag particles, would prevent visible light absorption of Ag_3PO_4 , which decreases the photocatalytic activity. To overcome this problem, AgX ($X = \text{Cl}, \text{Br}, \text{I}$), Ag nanoparticles and carbon quantum dots (CQDs), $g\text{-C}_3\text{N}_4/\text{Ag}_3\text{PO}_4$ hybrid photocatalyst were utilized to design some heterostructured nanocomposites with Ag_3PO_4 [12–16]. The AgX , Ag nanoparticles CQDs and $g\text{-C}_3\text{N}_4$ actually promotes the transfer and separation of photogenerated electron–hole pairs on Ag_3PO_4 particles, which eventually improves the stability of Ag_3PO_4 by decreasing the photocorrosion.

In recent years, modification of some semiconductor photocatalyst with graphene oxide (GO) has drawn much interest in the field of photocatalytic degradation of organic dyes [17–19]. Graphene has been recognized as versatile material to enhance photoinduced charge transfer for the improved photocatalytic activity of semiconductors [20–22]. It can thus perform as an ideal co-catalyst candidate for fabricating graphene-based semiconductor composite photocatalysts [22–25], hybrid composites of some conventional photocatalysts such as GO/ZnO [26,27], GO/TiO_2 [28] and $\text{GO}/\text{Ag}/\text{AgX}$ [29], $\text{Ag}_3\text{PO}_4/\text{GO}$ [30], $\text{Ag}_3\text{PO}_4/\text{GNS}$ [31], $\text{Ag}_3\text{PO}_4/\text{rGO}$ [32], $\text{Ag}_3\text{PO}_4/\text{rGO}$ [33] have been reported. In these hybrid composites, deposition of the photocatalysts in GO sheet increases their visible light absorption efficiency and the separation ratio of photogenerated electron–hole pairs have been greatly enhanced [23,24]. The technique of incorporating GO with conventional semiconductor photocatalysts improves the photocatalytic performance of the semiconductors by harnessing the cocatalyst role of GO to separate the photogenerated electrons and prevent the recombination of electron–hole pairs [20]. Using this concept, we have developed a modified reduced graphene oxide (RGO) based silver orthophosphate heterostructure nanocomposite by a simple sol-gel and hydrothermal method. The prepared material has been used for decolourization of Acid Blue 25 from water.

2. Experimental section

2.1. Materials and material synthesis

2.1.1. Materials

AgNO_3 procured from Merck KGaA (Germany) was used as the Ag^+ ion precursor. Acid Blue 25 [1-amino-9,10-dihydro-9,10-dioxo-4-(phenylamino)-2-anthracenesulfonic acid, monosodium salt] (C.I. number: 62055, molecular formula: $\text{C}_{20}\text{H}_{13}\text{N}_2\text{NaO}_5\text{S}$) was procured from Sigma-Aldrich (USA) and is used without further purification. All other solvents and chemicals used were of analytical grade.

2.1.2. Synthesis of graphene oxide

The GO was synthesized by modified Hummer's method [34]. In this method an acidified KMnO_4 solution was prepared by adding 9.0 g of KMnO_4 in 200 mL of 9:1 mixture of concentrated H_2SO_4 and H_3PO_4 . Then 1.5 g of graphite flakes was added to this solution under continuous stirring at 50°C for 12 h at 500 rpm. The reaction mixture was cooled to room temperature and poured onto 200 mL of ice cold distilled water containing 3 mL of 30% H_2O_2 . The mixture was then repeatedly centrifuged and washed successively with water, 30% HCl solution and ethanol. The solid product of GO thus obtained was finally dried at 80°C in an oven.

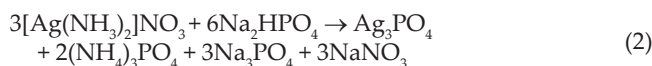
2.1.3. Synthesis of reduced graphene oxide

To synthesize RGO, 0.6 g of GO synthesized as above was dispersed in 100 mL distilled water and 0.1 g of NaBH_4 was added to the GO suspension. The mixture was then heated to 100°C for 24 h. The solid product thus obtained was centrifuged and washed repeatedly with distilled water. The product was finally dried at 80°C in an oven. The Schematic illustration of synthesis of GO and RGO were shown in Fig. 1.

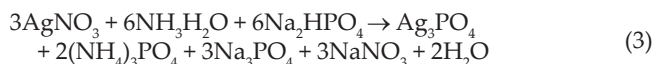
2.1.4. Synthesis of silver orthophosphate Ag_3PO_4

Silver orthophosphate (Ag_3PO_4) was prepared by using silver-amino complex as the Ag^+ ion source. 100 mL 0.2 M of ammonia aqueous solution was added drop by drop to 100 mL 0.1 M of AgNO_3 solution to form a transparent solution. 100 mL 0.2 M solution of Na_2HPO_4 was slowly added to the above solution with constant stirring and crystals of Ag_3PO_4 was obtained. The solid product is washed several times with distilled water and finally dried at 80°C in an oven.

Reaction involved:



Overall reaction:



2.1.5. Synthesis of $\text{GO-Ag}_3\text{PO}_4$ nanocomposite

In a typical synthesis, the as-made 155 mg of GO was dispersed in 100 mL distilled water and sonicated in a sonicator

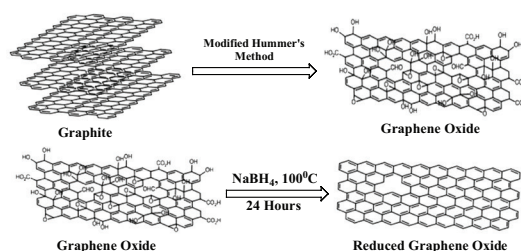


Fig. 1. Schematic illustration of synthesis of GO and RGO.

for 1 h to give a GO aqueous suspension (1.55 mg mL^{-1}). Now, 0.01 mol of AgNO_3 was added to the above GO suspension with constant stirring for 1 h to ensure an electrostatically driven assembly of Ag^+ ions on negatively charged sheets of GO. Then, 100 mL 0.2 M of ammonia aqueous solution was added slowly drop by drop to the above solution. After that, 100 mL 0.2 M solution of Na_2HPO_4 was added drop wise to the above solution with constant stirring. The mixture was stirred for further 30 min. The $\text{GO-Ag}_3\text{PO}_4$ nanocomposites were collected by filtration and drying in an oven at 80°C .

2.1.6. Synthesis of $\text{RGO-Ag}_3\text{PO}_4$ nanocomposite

To synthesize $\text{RGO-Ag}_3\text{PO}_4$ nanocomposite, the above mixed suspension was transferred to a Teflon-lined stainless steel autoclave and kept in an oven at 120°C for 4 h. After the hydrothermal treatment, the autoclave was allowed to cool naturally to room temperature. The solid $\text{RGO-Ag}_3\text{PO}_4$ products were washed several times with distilled water and were dried in an oven at 80°C . The Schematic diagram for the Synthesis of $\text{GO-Ag}_3\text{PO}_4$ and $\text{RGO-Ag}_3\text{PO}_4$ nanocomposites were shown in Fig. 2.

2.2. Characterization

Powder XRD pattern was recorded by Bruker AXS (Germany) X-ray powder diffractometer model D8 Focus using Cu K_α radiation with 2θ ranging from 10° to 80° with a step size of 0.020 . The FESEM images were taken by Zeiss FESEM Model Sigma (Germany). The Raman spectra were recorded by Renishaw (UK) Raman Spectrometer Model Renishaw Basis Series with 514 Lasers. FTIR spectra were obtained by PerkinElmer (USA) FTIR spectrometer Model C-107727 in the range $450\text{--}4,000 \text{ cm}^{-1}$. The diffuse reflectance spectra were recorded by Varian Cary UV-VIS NIR spectrophotometer model 5000 equipped with diffuse reflectance accessory in wavelength range of $200\text{--}800 \text{ nm}$ with BaSO_4 as reference. The photoluminescence (PL) spectra were obtained by PerkinElmer (USA) fluorescence spectrometer model LS 55 with an excitation at 350 nm . The BET surface area of the nanocomposite is obtained by nitrogen adsorption method using BET equation at 77 K with the help of Quantachrome Autosorb-1C Surface Area Analyzer.

2.3. Photocatalytic activity

In a typical reaction, 200 mL of $20 \mu\text{mol/L}$ dye solution was taken in a double-jacketed photocatalytic glass reactor

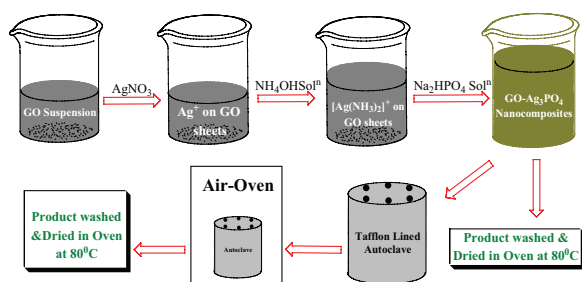


Fig. 2. Schematic diagram for the synthesis of $\text{GO-Ag}_3\text{PO}_4$ and $\text{RGO-Ag}_3\text{PO}_4$ nanocomposite.

(borosilicate) and 250 mg of the catalyst was added to it. The photocatalytic reactor with the solution was placed on a magnetic stirrer and kept in dark with constant stirring to achieve an adsorption–desorption equilibrium. After 60 min, the dye solution was illuminated with visible light by a halogen bulb (24V 250 watt 7748Xhp G6.35 , Philips, India) fitted with a glass filter to cut-off short wavelengths ($\lambda < 420 \text{ nm}$) [35]. The concentration of the dye solution after attaining adsorption–desorption equilibrium was considered as the initial concentration. 5 mL of the dye solution were then collected at a regular time intervals, centrifuged by Remi Centrifuged machine model R 24 and the concentration of the dye was measured by visible spectrometer (Elico (India), model SL-177) at $\lambda_{\text{max}} = 600 \text{ nm}$.

The percentage degradation was determined by the equation:

$$\%D = \frac{C_0 - C_t}{C_0} \times 100 \quad (4)$$

where C_0 and C_t are the initial concentration and concentration of the dye solution at time t , respectively.

2.4. Adsorption study

To compare the adsorption capabilities of the composites synthesized, the adsorption of Acid Blue 25 on Ag_3PO_4 , $\text{GO-Ag}_3\text{PO}_4$ and $\text{RGO-Ag}_3\text{PO}_4$ were tested by mixing 50 mg of the catalyst with 50 mL of dye solution in 100 mL Erlenmeyer flasks in a constant temperature water bath thermostat shaker for 60 min under dark. The unadsorbed supernatant liquid was decanted from one flask after regular time intervals, centrifuged and then the concentration of the dye was determined with the help of visible spectrometer. The percentage adsorption also was determined by using the equation that as in case of % degradation.

2.5. Percentage mineralization

The photocatalytic degradation of the dye studied was followed by examination of the maximum reduction of the carbon content in the dye solution by estimating the chemical oxygen demand (COD) by spectrophotometric method [36]. The reduction of COD values confirms the degradation of organic pollutants in water. The % efficiency of the photocatalytic degradation was calculated by the following equation:

$$\% \text{ Efficiency } (\eta) = \frac{(\text{Initial COD} - \text{Final COD})}{\text{Initial COD}} \times 100 \quad (5)$$

3. Results and discussion

3.1. Characterization of the photocatalyst

The powder XRD patterns of GO, RGO, Ag_3PO_4 , $\text{GO-Ag}_3\text{PO}_4$ and $\text{RGO-Ag}_3\text{PO}_4$ are shown in Fig. 3. A characteristic peak of $(0\ 0\ 2)$ at $2\theta = 11^\circ$ reveal the conversion of graphite to GO [37]. The peak due to $(0\ 0\ 2)$ is disappeared and a broad peak $2\theta = 25^\circ$ is seen in RGO which confirms the conversion of GO to RGO [37].

The formation of Ag_3PO_4 is confirmed by the XRD pattern of Ag_3PO_4 which reveals body centred cubic (bcc) structure (JCPDS No. 06-0505) which is in accordance with previous results [38]. $\text{GO-Ag}_3\text{PO}_4$ and $\text{RGO-Ag}_3\text{PO}_4$ shows similar XRD pattern as those of bare Ag_3PO_4 which suggest grafting of Ag_3PO_4 particles on GO and RGO sheets, but the characteristic peak of GO at $2\theta = 11^\circ$ and RGO at $2\theta = 25^\circ$ are not found due to very low diffraction intensity of GO and RGO as compared with Ag_3PO_4 . The particle size was calculated from (210) (211) and (320) peaks by using Scherrer equation:

$$D = k\lambda/\beta\cos\theta \quad (6)$$

where $k = 0.94$ for crystals with cubic symmetry, $\lambda = 0.154$ nm, β = full width half maxima and θ = diffraction angle. The

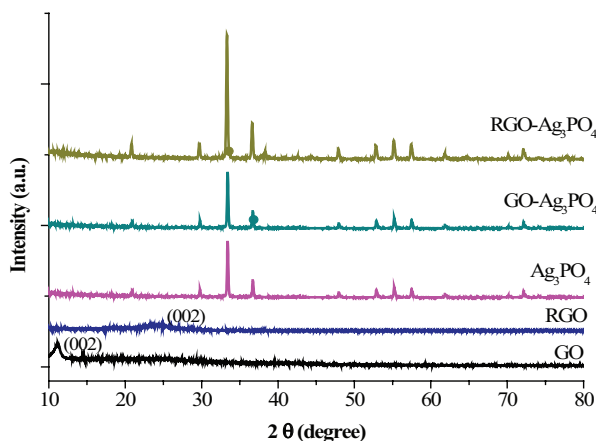


Fig. 3. Powder XRD pattern of GO, RGO, Ag_3PO_4 , $\text{GO-Ag}_3\text{PO}_4$ and $\text{RGO-Ag}_3\text{PO}_4$.

average particle size for Ag_3PO_4 , $\text{GO-Ag}_3\text{PO}_4$ and $\text{RGO-Ag}_3\text{PO}_4$ was found to be 60, 54 and 46 nm, respectively.

Fig. 4 depicts the XPS spectra of C 1s of GO and that of $\text{RGO-Ag}_3\text{PO}_4$ composite. In the C 1s of GO, two intense peaks are observed, one at binding energy of 283 eV due to graphitic carbon and other one at 286.6 eV due to hydroxyl C–OH. Whereas the intensity of the later goes on decreasing due to the removal of the functional groups containing oxygen during the hydrothermal synthesis. This reveals that reduction of GO to RGO is achieved [39].

The FESEM images of the as-prepared samples are shown in Fig. 5. The FESEM image (Fig. 5(a)) reveals that GO has sheet-like structure which may provide enough surface area for adsorption.

The FESEM image of bare Ag_3PO_4 (Fig. 4(b)) shows that the compound has varying sizes. The Ag_3PO_4 nanoparticles

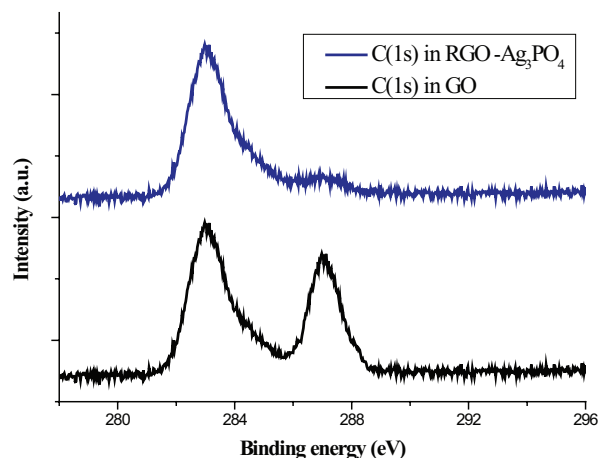


Fig. 4. XPS spectrum of C 1s in GO and $\text{RGO-Ag}_3\text{PO}_4$ composite.

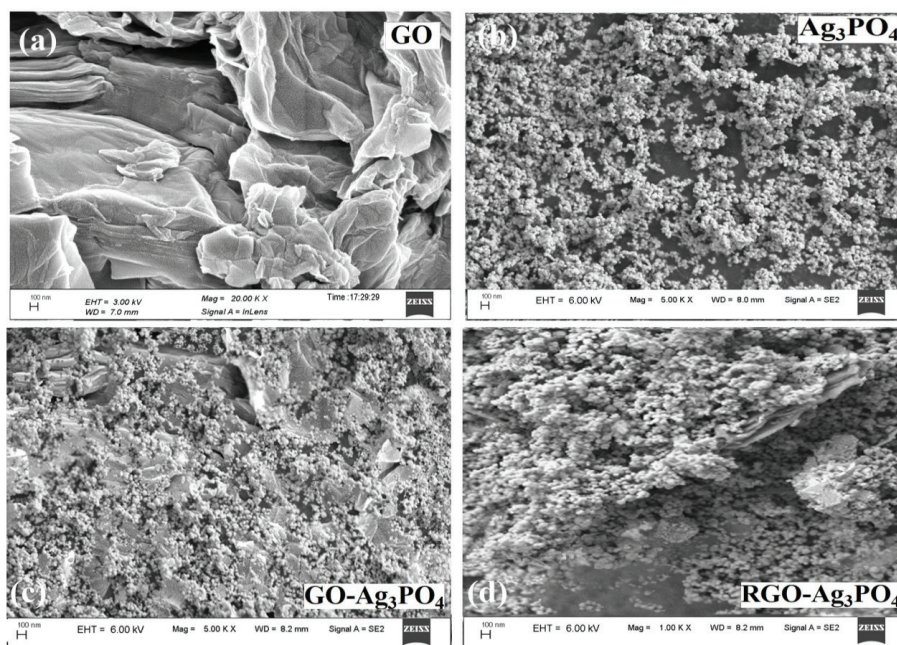


Fig. 5. FESEM image of GO, Ag_3PO_4 , $\text{GO-Ag}_3\text{PO}_4$ and $\text{RGO-Ag}_3\text{PO}_4$.

are distributed on the GO sheets as seen in Fig. 4(c). The FESEM image of RGO-Ag₃PO₄ (Fig. 5(d)) implied that hydrothermal treatment of the GO-Ag₃PO₄ composites convert GO to RGO with slight decrease in size of Ag₃PO₄ particles. Fig. 6 shows the energy dispersive spectroscopy elemental microanalysis of Ag₃PO₄ and RGO-Ag₃PO₄. The peak corresponding to Ag, P and O elements in Fig. 6(a) indicates the formation of Ag₃PO₄ while that corresponding to C of GO in Figs. 6(b) and (c) confirms that GO-Ag₃PO₄ and RGO-Ag₃PO₄ composites were successfully synthesized in this study. From the analysis of the wt%, it is found that the ratio of Ag to P is close the chemical composition of Ag₃PO₄. The GO contents of the GO-Ag₃PO₄ and RGO-Ag₃PO₄ composites were found to be around 10% (w/w).

The average particle size was found to be 60 nm, 50 nm and around 50 nm in bare Ag₃PO₄, GO-Ag₃PO₄ and RGO-Ag₃PO₄ as calculated from the histogram plots as shown in Fig. 7 which is in agreement with that calculated by Scherrer equation from XRD data.

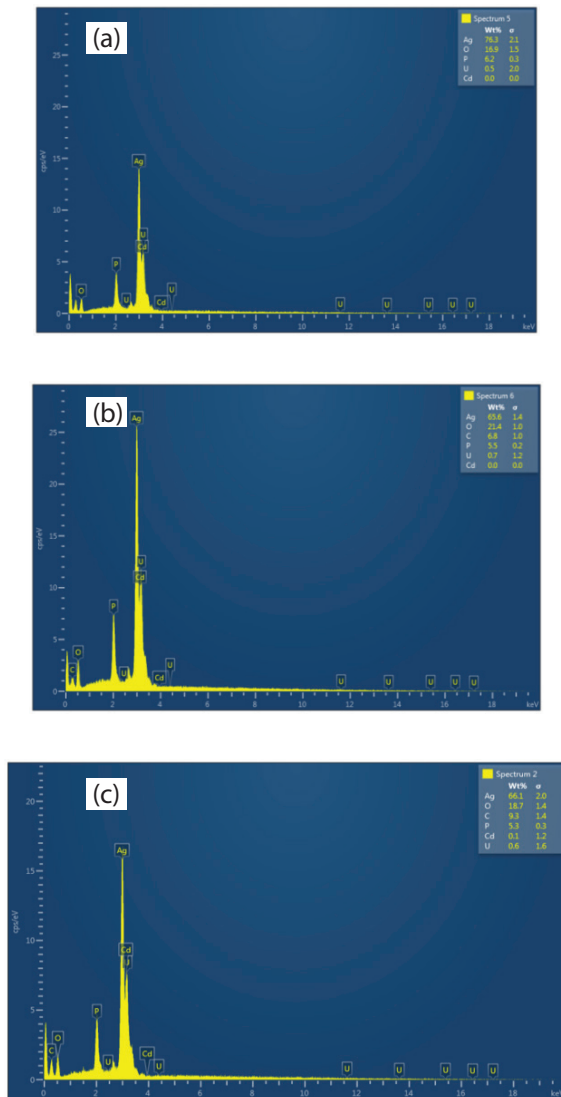


Fig. 6. Energy dispersive spectroscopy (EDS) pattern of (a) Ag₃PO₄, (b) GO-Ag₃PO₄ and (c) RGO-Ag₃PO₄.

Fig. 8 displays the FTIR spectra of the GO, RGO, Ag₃PO₄, GO-Ag₃PO₄ and RGO-Ag₃PO₄. In the FTIR spectra of GO, characteristic peaks at 1,720; 1,630 and 1,058 cm⁻¹ corresponds

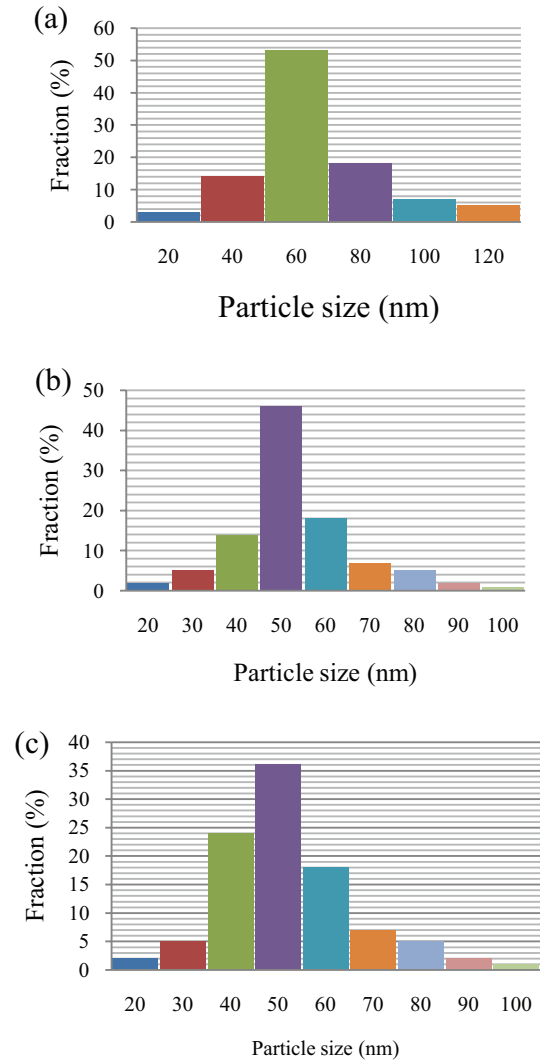


Fig. 7. Histogram plot showing particle size distribution from SEM images of (a) Ag₃PO₄, (b) GO-Ag₃PO₄ and (c) RGO-Ag₃PO₄.

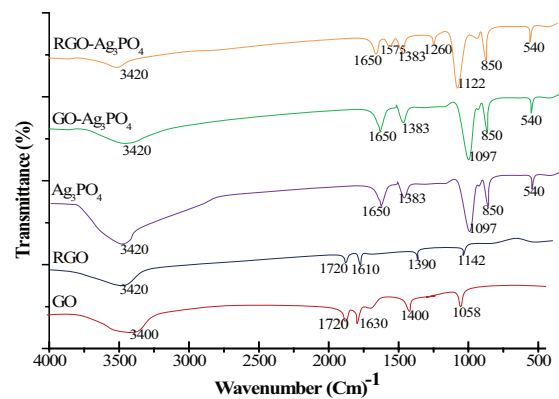


Fig. 8. FTIR spectra of the GO, RGO, Ag₃PO₄, GO-Ag₃PO₄ and RGO-Ag₃PO₄.

to stretching vibrations of carboxylic C=O, C=C and alkoxy C–O [40], respectively, with a broad absorption peak centred around $3,400\text{ cm}^{-1}$ and another one at $1,630\text{ cm}^{-1}$ are due to O–H stretching vibrations [41]. In case of RGO, the absorption peak at $1,720\text{ cm}^{-1}$ corresponds to stretching vibration of carboxylic C=O. The peak centred around $1,610$ and a broad peak at $3,420\text{ cm}^{-1}$ correspond to bending vibrations of –OH and stretching vibrations of the RGO sheets, respectively [6]. At $1,390\text{ cm}^{-1}$ another peak is seen which is attributed to the tertiary C–OH group stretching vibration [42]. The absorption peak at $1,142\text{ cm}^{-1}$ is related to the stretching vibration of C–O–C of epoxy and alkoxy groups in RGO. In the FTIR spectra of bare Ag_3PO_4 , the absorption peak at 540 cm^{-1} corresponds to O=P–O bending vibrations, peak at 850 and $1,097\text{ cm}^{-1}$ correspond to symmetric and asymmetric stretching vibrations of P–O–P rings [6]. The peak at $1,383\text{ cm}^{-1}$ is attributed to the stretching mode of vibrations of P=O [43]. In addition to these, two peaks at $1,650$ and $3,420\text{ cm}^{-1}$ are observed due to the –OH bending and stretching vibrations of H_2O molecules adsorbed [43]. Similar peaks are observed in the as-synthesized $\text{GO-Ag}_3\text{PO}_4$. In the FTIR spectra of $\text{RGO-Ag}_3\text{PO}_4$, two new peaks are observed a $1,260$ and $1,575\text{ cm}^{-1}$ which corresponds to the skeletal vibration of GO sheets and C–O stretching vibration of epoxy C–O–C which reveals the conversion of GO to RGO [6]. While the peak at $1,122\text{ cm}^{-1}$ corresponds to the stretching vibrations of P–O–P group instead of $1,097\text{ cm}^{-1}$ as observed in bare Ag_3PO_4 which suggest that the Ag_3PO_4 particles strongly interact with the RGO sheets [43].

Fig. 9 shows the Raman spectra of GO, RGO, Ag_3PO_4 , $\text{GO-Ag}_3\text{PO}_4$ and $\text{RGO-Ag}_3\text{PO}_4$. In the Raman spectra two bands are seen at around $1,340$ and $1,600\text{ cm}^{-1}$ which attributed to disordered sp^2 carbon (D-band) and ordered graphite (G-band), respectively. In case of RGO, same peaks are observed but the I_D/I_G ratio is increased to 0.96 as compared with that of 0.85 in GO which is in agreement with previous results [38].

This reveals that reduction of GO to RGO is achieved. For bare Ag_3PO_4 , a peak at around 912 cm^{-1} is seen which corresponds to the PO_4^{3-} symmetric stretching vibrations [44]. In the Raman spectra of $\text{GO-Ag}_3\text{PO}_4$ both the D and G bands are seen ($I_D/I_G = 0.85$) in addition to the peak at around 912 cm^{-1} due to the PO_4^{3-} symmetric stretching vibrations of

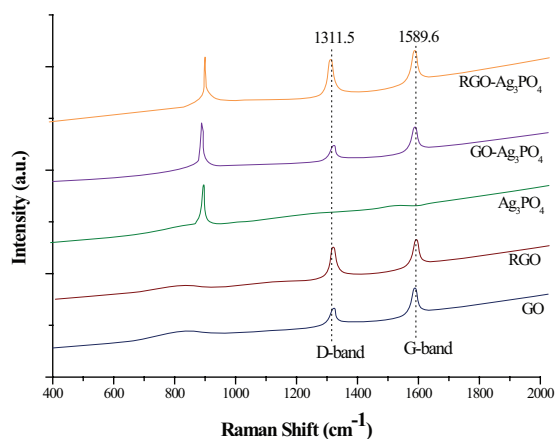


Fig. 9. Ramanspectraof GO, Ag_3PO_4 , $\text{GO-Ag}_3\text{PO}_4$ and $\text{RGO-Ag}_3\text{PO}_4$.

Ag_3PO_4 . In $\text{RGO-Ag}_3\text{PO}_4$, similar peaks are seen at $1,311.5$ and $1,589.6\text{ cm}^{-1}$ with $I_D/I_G = 0.96$. The position of the G band (in wave numbers) provides information about the number of layers in GO and RGO and that can be calculated by using the following equation [45]:

$$W_G = 1581.6 + 11/(1 + n^{1.6}) \quad (7)$$

where W_G is the position of the G band (in wave number), W_C is the number of layers and the number $1,581.6\text{ cm}^{-1}$ is the position of the sharp peak in the Raman spectra of graphite. The average number of layers in RGO is thus found to be 1.67 (~2 or bilayer) as calculated by using the above equation. The result of Raman spectra also confirms the presence of GO and RGO in $\text{GO-Ag}_3\text{PO}_4$ and $\text{RGO-Ag}_3\text{PO}_4$, respectively.

The DRS of Ag_3PO_4 , $\text{GO-Ag}_3\text{PO}_4$ and $\text{RGO-Ag}_3\text{PO}_4$ are shown in Fig. 10. The spectra show that the visible light absorption enhances for $\text{GO-Ag}_3\text{PO}_4$ and $\text{RGO-Ag}_3\text{PO}_4$ composites as compared with bare Ag_3PO_4 .

The band gap (E_g) is calculated using the equation $E_g = 1240/\lambda$ [46], where λ is the wavelength corresponding to the point of intersection between vertical and horizontal lines in the spectra. The E_g value of Ag_3PO_4 , $\text{GO-Ag}_3\text{PO}_4$ and $\text{RGO-Ag}_3\text{PO}_4$ is found to be 2.45 , 2.33 and 2.29 eV , respectively. The narrowing of the band gap from the DRS reveals that when Ag_3PO_4 is grafted on GO and RGO sheets, the photocatalytic activity of the material increases.

Fig. 11 displays the PL spectra of bare Ag_3PO_4 , $\text{GO-Ag}_3\text{PO}_4$ and $\text{RGO-Ag}_3\text{PO}_4$. A sharp emission peak at around 600 nm is observed on excitation at 350 nm .

The Ag_3PO_4 particles when deposited on GO sheets, the PL intensity decreases. On hydrothermal treatment of the $\text{GO-Ag}_3\text{PO}_4$ composite, the PL intensity decreases sharply which indicates that the recombination of the photogenerated charge carriers is diminished. This implies that the nanocomposite can be effectively used in photocatalysis [47].

BET specific surface area of bare Ag_3PO_4 and $\text{RGO-Ag}_3\text{PO}_4$ is found to be 3.3 and $7.835\text{ m}^2\text{ g}^{-1}$, respectively. While that of GO sheets is $31.4\text{ m}^2\text{ g}^{-1}$. Thus it is confirmed that the incorporation of GO with Ag_3PO_4 results in increase in surface area of $\text{RGO-Ag}_3\text{PO}_4$ composites.

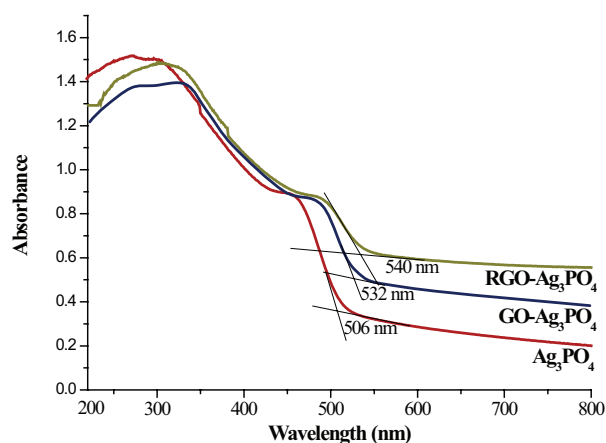


Fig. 10. DRS of Ag_3PO_4 , $\text{GO-Ag}_3\text{PO}_4$ and $\text{RGO-Ag}_3\text{PO}_4$.

3.2. Photocatalytic activity of the material

Fig. 12 shows the photocatalytic degradation of bare Ag_3PO_4 , $\text{GO-Ag}_3\text{PO}_4$ and $\text{RGO-Ag}_3\text{PO}_4$ with Acid Blue 25 dye with an initial concentration of $20 \mu\text{mol/L}$. For comparison, a blank test with constant stirring was also performed.

The degradation of Acid Blue 25 in the absence of the catalyst was found to be negligible which confirms that self degradation of the dye is not feasible. The bare Ag_3PO_4 showed weak photocatalytic activity with a degradation percentage of 55.4% after equilibrium is achieved at 90 min of visible light illumination. The $\text{GO-Ag}_3\text{PO}_4$ composite exhibits better photocatalytic activity with a degradation percentage of 68.8%. The hydrothermally obtained $\text{RGO-Ag}_3\text{PO}_4$ composite has the highest photocatalytic degradation percentage of 82%. The result reveals that when Ag_3PO_4 particles are grafted on GO and RGO sheets, the photocatalytic performance was enhanced to a considerable extent.

Fig. 13 depicts the UV–Vis absorption spectral changes of Acid Blue 25 dye degradation in aqueous medium under visible light with $\text{RGO-Ag}_3\text{PO}_4$ composite synthesized by hydrothermal method. The spectra shows that with increase in degradation time, the absorption maxima at $\lambda_{\text{max}} = 600 \text{ nm}$ goes on decreasing and after 90 min of degradation it almost completely disappeared.

The colour change of the dye solution degraded in aqueous medium under visible light irradiation with

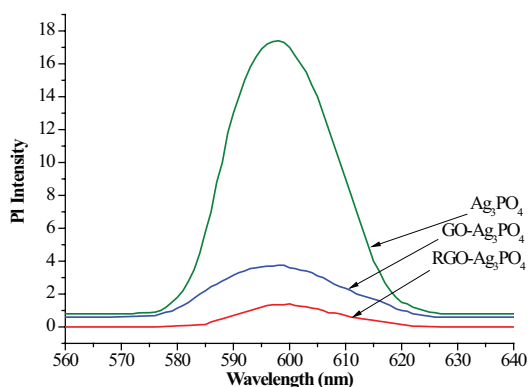


Fig. 11. Photoluminescence (PL) spectra of bare Ag_3PO_4 , $\text{GO-Ag}_3\text{PO}_4$ and $\text{RGO-Ag}_3\text{PO}_4$.

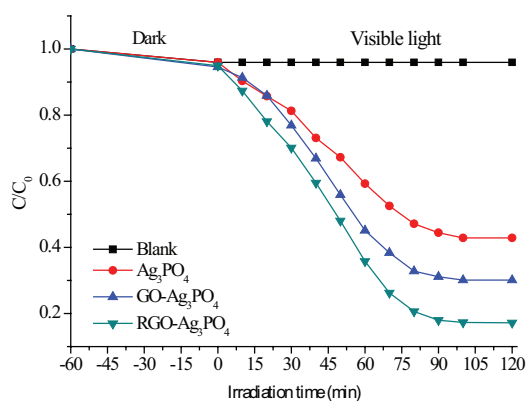


Fig. 12. Photocatalytic degradation of bare Ag_3PO_4 , $\text{GO-Ag}_3\text{PO}_4$ and $\text{RGO-Ag}_3\text{PO}_4$.

$\text{RGO-Ag}_3\text{PO}_4$ composite after regular time interval is shown in Fig. 14. Decolourization of the dye solution was achieved almost completely after 90 min and equilibrium is achieved.

3.3. Kinetic study of the photocatalytic degradation

The kinetics of the degradation of Acid Blue 25 dye was studied by modified Langmuir–Hinshelwood (L–H) mechanism which could be expressed as:

$$\ln(C_0/C) = kt \quad (8)$$

where k is the overall rate constant in min^{-1} . The plot of $\ln(C_0/C)$ against irradiation time (min) for the photocatalysts (Fig. 15) give straight lines which reveal that the degradation of Acid Blue 25 follows pseudo-first order kinetics.

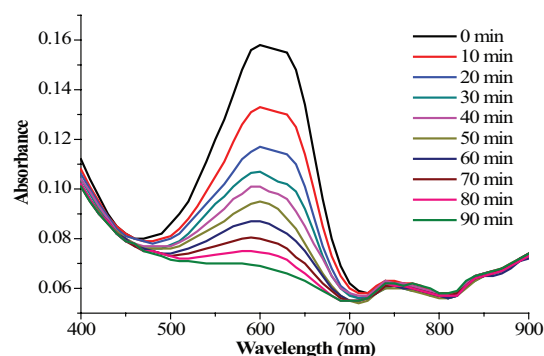


Fig. 13. UV–Vis spectral changes of Acid Blue 25 dye degradation in aqueous medium under visible light using $\text{RGO-Ag}_3\text{PO}_4$ composite.



Fig. 14. Change in colour of Acid Blue 25 dye degradation in aqueous medium under visible light using $\text{RGO-Ag}_3\text{PO}_4$ composite.

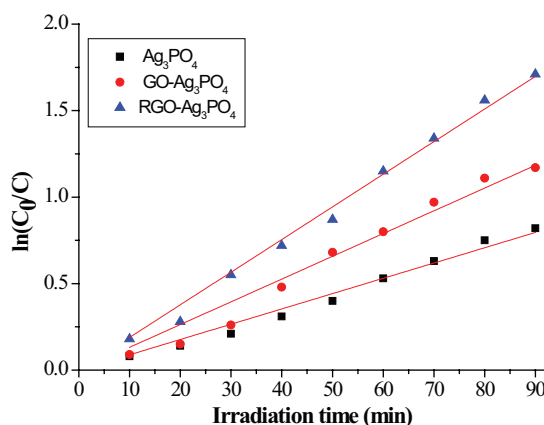


Fig. 15. Plot of $\ln(C_0/C)$ against irradiation time (min).

From the analysis of the plot, the Langmuir–Hinshelwood rate constant (k), first order kinetic equation and relative coefficient (R^2) for the degradation of Acid Blue 25 under visible light illumination were determined and are shown in Table 1.

The rate constant (min^{-1}) for each photocatalyst was obtained from the slopes of the straight line obtained through regression. The rate constant k (min^{-1}) for bare Ag_3PO_4 was found to be $08.48 \times 10^{-3} \text{ min}^{-1}$ which has increased to $13.15 \times 10^{-3} \text{ min}^{-1}$ and $18.87 \times 10^{-3} \text{ min}^{-1}$ in $\text{GO-Ag}_3\text{PO}_4$ and $\text{RGO-Ag}_3\text{PO}_4$ respectively.

3.4. Adsorption study

For better photocatalytic performance, the dye particles must be adsorbed on the surface of the catalyst. To understand the extent of adsorption of the dye on Ag_3PO_4 , $\text{GO-Ag}_3\text{PO}_4$ and $\text{RGO-Ag}_3\text{PO}_4$, the adsorption capabilities were studied (Fig. 16) and it is found that the adsorption of $\text{GO-Ag}_3\text{PO}_4$ (27.7%) and $\text{RGO-Ag}_3\text{PO}_4$ composites (31.8%) were (20.5%) much higher than the bare Ag_3PO_4 . Similar results were also obtained with N-doped TiO_2 photocatalyst (34.4%) with a catalyst load of 1.0 g/L and N- TiO_2 -RGO nano-composite (12.24%) with catalyst load of 0.75 g/L for the same period of time [8,48].

3.5. Mineralization of dye

The extent of mineralization was examined in terms of the decrease in COD value. In the present study, 200 mL of 20 $\mu\text{mol/L}$ dye solution was taken in the photocatalytic reactor with 250 mg of the $\text{RGO-Ag}_3\text{PO}_4$ catalyst and it was observed that there is a steady decrease in the COD value (Fig. 17(a)) and increase in % efficiency, η (Fig. 17(b)) with increase in the visible light irradiation time. The η value increased from 8.35% to 84.75% during irradiation of light up to 120 min. After 90 min of visible light irradiation, the η value was found to be 78.26% whereas at the same time the % degradation was 82%. The mineralization % efficiency (η) was found to be lower than the % degradation. This might be attributed to the formation of some smaller uncoloured products which contributes to the increased COD values.

3.6. Mechanism

In $\text{GO-Ag}_3\text{PO}_4$ composite, GO expands the light absorption range, enhances adsorption of the dye particles due to increased surface area and also reduces photocorrosion of Ag_3PO_4 [25,27]. The combining merits of Ag_3PO_4 and GO results in the enhancement of the photocatalytic activity under visible light when Ag_3PO_4 is tailored on the surface of GO sheets [30]. A probable mechanism for the increased

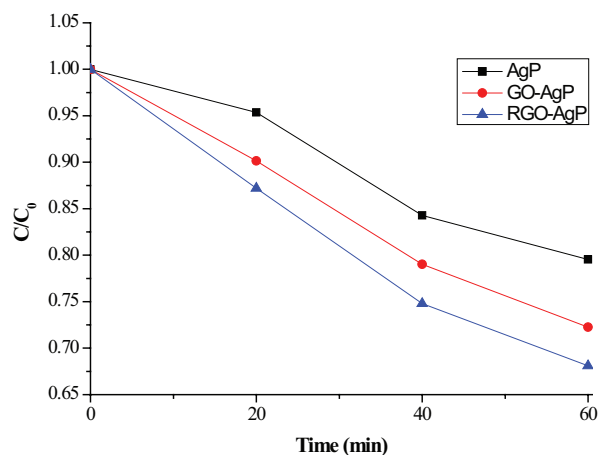


Fig. 16. Adsorption capabilities of Acid Blue 25 on Ag_3PO_4 , $\text{GO-Ag}_3\text{PO}_4$ and $\text{RGO-Ag}_3\text{PO}_4$.

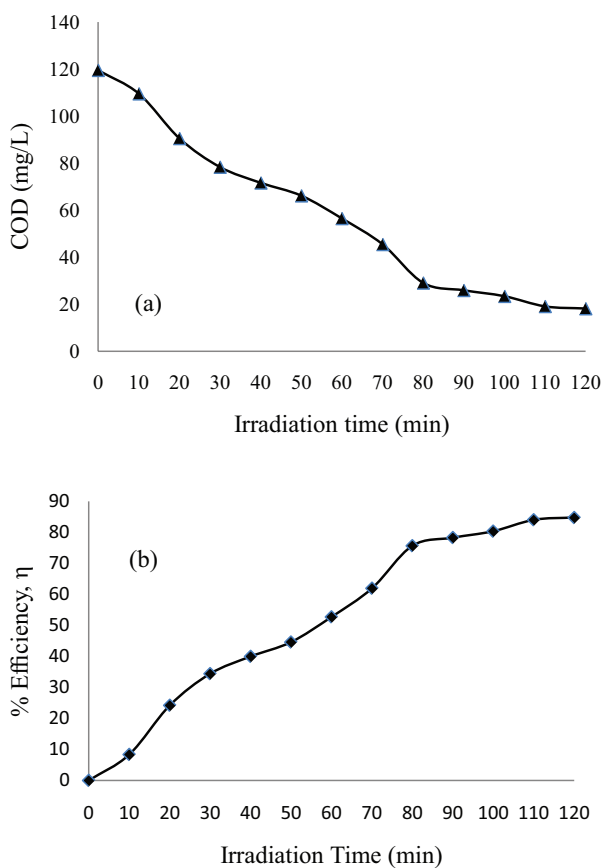


Fig. 17. Variation of (a) COD with irradiation time and (b) % mineralization (η) with irradiation time.

Table 1

Langmuir–Hinshelwood rate constant (k), first order kinetic equation and relative coefficient (R^2)

Catalyst	First order kinetic equation	Langmuir–Hinshelwood rate constant (k) in min^{-1}	R^2
Ag_3PO_4	$\ln(C_0/C) = 0.00848t$	08.48×10^{-3}	0.9946
$\text{GO-Ag}_3\text{PO}_4$	$\ln(C_0/C) = 0.01315t$	13.15×10^{-3}	0.9906
$\text{RGO-Ag}_3\text{PO}_4$	$\ln(C_0/C) = 0.01887t$	18.87×10^{-3}	0.9978

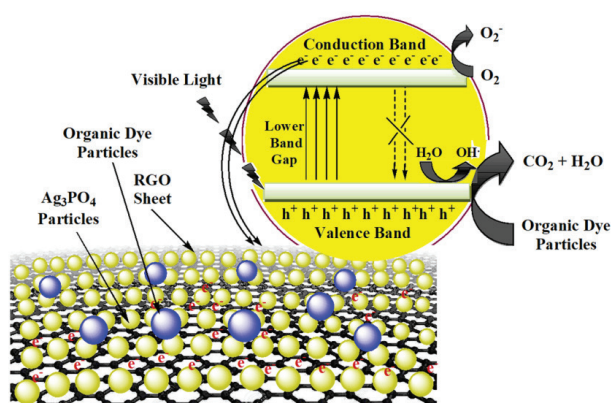


Fig. 18. Photocatalytic degradation mechanism.

photocatalytic activity of the RGO- Ag_3PO_4 nanocomposite over bare Ag_3PO_4 is proposed in this study as shown in Fig. 18. When visible light having energy higher than the band gap energy of falls on Ag_3PO_4 , the electrons in the valence band (VB) are excited to the higher energy conduction band (CB) leaving behind holes. The electrons in the CB are then quickly transferred to RGO sheets and react with dissolved O_2 to form O_2^- ions which further reacts with hydrogen ions to produce HO_2 radicals. The HO_2 along with H^+ ions combine with electrons to generate H_2O_2 . The holes in the VB are highly oxidizing which readily oxidizes donor molecules and react with water to form OH radicals. These OH radicals along with HO_2 and O_2^- are responsible for the degradation of the dye.

4. Conclusion

The result revealed that heterostructure nanocomposite of silver orthophosphate (Ag_3PO_4) grafted on RGO sheets could be easily synthesized by simple sol-gel and hydrothermal method. The photocatalytic decolorization of Acid Blue 25 dye followed pseudo-first order kinetics, which can be fitted the modified Langmuir–Hinshelwood model. The degradation results showed that RGO- Ag_3PO_4 composite has higher degradation percentage than the GO- Ag_3PO_4 composite. Thus the photocatalytic activity of silver orthophosphate was greatly enhanced when integrated with RGO and the enhanced photocatalytic activity is ascribed to the higher adsorption and small sized well dispersed Ag_3PO_4 particles on GO as well as RGO sheets.

Acknowledgements

The authors gratefully acknowledge SAIC, Tezpur University, SAIF, Guwahati University, CIF, IIT Guwahati, Assam and CSIR-CERI, Karaikudi, Tamil Nadu, India, for various characterization of the materials.

References

[1] L. Muszkat, D. Raucher, M. Magaritz, D. Ronen, in *U. Zoller, Ed., Groundwater Contamination and Control*, Dekker, New York, 1994, pp. 257–272.
 [2] R.M. Dowd, M.P. Anderson, M.L. Johnson, Proceedings of the 2nd National Outdoor Action Conference on Aquifer

Restoration, Groundwater. Monitoring Geophysical Methods, National Water Well Association, Dublin, OH, 1998, pp. 1365–1379.
 [3] V.K. Gupta, Suhas, Application of low-cost adsorbents for dye removal—a review, *J. Environ. Manage.*, 90 (2009) 2313–2342
 [4] X.B. Chen, S.H. Shen, L.J. Guo, S.S. Mao, Semiconductor based photocatalytic hydrogen generation, *Chem. Rev.*, 110 (2010) 6503–6570.
 [5] S. Navalon, A. Dhakshinamoorthy, M. Alvaro, H. Garcia, Photocatalytic CO_2 reduction using non-titanium metal oxides and sulfides, *Chem. Sust. Chem.*, 6 (2013) 562–577.
 [6] B. Chai, J. Li, Q. Xu, Reduced graphene oxide grafted Ag_3PO_4 composites with efficient photocatalytic activity under visible-light irradiation, *Ind. Eng. Chem. Res.*, 53 (2014) 8744–8752.
 [7] J. Cao, B.D. Luo, H.L. Lin, B.Y. Xu, S.F. Chen, Visible light photocatalytic activity enhancement and mechanism of $\text{AgBr}/\text{Ag}_3\text{PO}_4$ hybrids for degradation of methyl orange, *J. Hazard. Mater.*, 217–218 (2012) 107–115.
 [8] D. Chakraborty, S.S. Gupta, Photo-catalytic decolorization of toxic dye with N-doped titania: a case study with Acid Blue 25, *J. Environ. Sci.*, 25 (2013) 1034–1043.
 [9] Y. Bi, H. Hu, S. Ouyang, G. Lu, J. Cao, J. Ye, Photocatalytic and photoelectric properties of cubic Ag_3PO_4 sub-microcrystals with sharp corners and edges, *Chem. Commun.*, 48 (2012) 3748–3750.
 [10] W. Yao, B. Zhang, C. Huang, C. Ma, X. Song, Q. Xu, Synthesis and characterization of high efficiency and stable $\text{Ag}_3\text{PO}_4/\text{TiO}_2$ visible light photocatalyst for the degradation of methylene blue and rhodamine B solutions, *J. Mater. Chem.*, 22 (2012) 4050–4055.
 [11] Y.P. Bi, S.X. Ouyang, J.Y. Cao, J.H. Ye, Facile synthesis of rhombic dodecahedral $\text{AgX}/\text{Ag}_3\text{PO}_4$ ($X = \text{Cl Br, I}$) heterocrystals with enhanced photocatalytic properties and stabilities, *Phys. Chem. Chem. Phys.*, 13 (2011) 10071–10075.
 [12] H.C. Zhang, H. Huang, H. Ming, H.T. Li, L.L. Zhang, Y. Liu, Z.H. Kang, Carbon quantum dots/ Ag_3PO_4 complex photocatalysts with enhanced photocatalytic activity and stability under visible light, *J. Mater. Chem.*, 22 (2012) 10501–10506.
 [13] H. Katsumata, T. Sakai, T. Suzuki, S. Kaneco, Highly efficient photocatalytic activity of g- $\text{C}_3\text{N}_4/\text{Ag}_3\text{PO}_4$ hybrid photocatalysts through Z-scheme photocatalytic mechanism under visible light, *Ind. Eng. Chem. Res.*, 53 (2014) 8018–8025.
 [14] Y. Liu, L. Fang, H. Lu, L. Liu, H. Wang, C. Hu, Highly efficient and stable $\text{Ag}/\text{Ag}_3\text{PO}_4$ plasmonic photocatalyst in visible light, *Catal. Commun.*, 17 (2012) 200–204.
 [15] Y. Liu, L. Fang, H. Lu, Y. Li, C. Hu, H. Yu, One-pot pyridine-assisted synthesis of visible-light-driven photocatalyst $\text{Ag}/\text{Ag}_3\text{PO}_4$, *Appl. Catal. B*, 115–116 (2012) 245–252.
 [16] L. Liu, J.C. Liu, D.D. Sun, Graphene oxide enwrapped Ag_3PO_4 composite, towards a highly efficient and stable visible light-induced photocatalyst for water purification, *Catal. Sci. Technol.*, 2 (2012) 2525–2532.
 [17] H. Zhang, X.J. Lv, Y.M. Li, Y. Wang, J.H. Li, P25-graphene composite as a high performance photocatalyst, *ACS Nano*, 4 (2010) 380–386.
 [18] J. Liu, H. Bai, Y. Wang, Z. Liu, X. Zhang, D. D. Sun, Self-assembling TiO_2 nanorods on large graphene oxide sheets at a two-phase interface and their anti-recombination in photocatalytic applications, *Adv. Funct. Mater.*, 20 (2010) 4175–4181.
 [19] C. Chen, W.M. Cai, M.C. Long, B.X. Zhou, Y.H. Wu, D.Y. Wu, Y.J. Feng, Synthesis of visible-light responsive graphene oxide/ TiO_2 composites with p/n heterojunction, *ACS Nano*, 4 (2010) 6425–6432.
 [20] N. Zhang, M. Yang, S. Liu, Y. Sun, Y. Xu, Waltzing with the versatile platform of graphene to synthesize composite photocatalysts, *Chem. Rev.*, 115 (2015) 10307–10377.
 [21] M.Q. Yang, N. Zhang, M. Pagliaro, Y.J. Xu, Artificial photosynthesis over graphene-semiconductor composites. Are we getting better?, *Chem. Soc. Rev.*, 43 (2014) 8240–8254.
 [22] C. Han, N. Zhang, Y.J. Xu, Structural diversity of graphene materials and their multifarious roles in heterogeneous photocatalysis, *Nano Today*, 11 (2016) 351–372.
 [23] X. Huang, Z. Yin, S. Wu, X. Qi, Q. He, Q. Zhang, Q. Yan, F. Boey, H. Zhang, Graphene-based materials: synthesis,

- characterization, properties, and applications, *Small*, 7 (2011) 1876–1902.
- [24] C. Han, Z. Chen, N. Zhang, J.C. Colmenares, Y.J. Xu, Hierarchically CdS decorated 1D ZnO nanorods-2D graphene hybrids: low temperature synthesis and enhanced photocatalytic performance, *Adv. Funct. Mater.*, 25 (2015) 221–229.
- [25] N.L. Yang, J. Zhai, D. Wang, Y.S. Chen, L. Jiang, Two-dimensional graphene bridges enhanced photoinduced charge transport in dye-sensitized solar cells, *ACS Nano*, 4 (2010) 887–894.
- [26] T.G. Xu, L.W. Zhang, H.Y. Cheng, Y.F. Zhu, Significantly enhanced photocatalytic performance of ZnO via graphene hybridization and the mechanism study, *Appl. Catal. B*, 101 (2011) 382–387.
- [27] B.X. Li, T.X. Liu, Y.F. Wang, Z.F. Wang, ZnO/graphene-oxide nanocomposite with remarkably enhanced visible-light-driven photocatalytic performance, *J. Colloid Interface Sci.*, 377 (2012) 114–121.
- [28] J. Liu, L. Liu, H. Bai, Y. Wang, D.D. Sun, Gram-scale production high-activity of graphene Oxide-TiO₂ nanorod composite: towards high activity photocatalytic materials, *Appl. Catal. B*, 106 (2011) 76–82.
- [29] M. Zhu, P. Chen, M. Liu, Graphene oxide enwrapped Ag/AgX (X = Br, Cl) nanocomposite as a highly efficient visible light plasmonic photocatalyst, *ACS Nano*, 5 (2011) 4529–4536.
- [30] G.D. Chen, M. Sun, Q. Wei, Y.F. Zhang, B.C. Zhu, B. Du, Ag₃PO₄/graphene-oxide composite with remarkably enhanced visible-light-driven photocatalytic activity toward dyes in water, *J. Hazard. Mater.*, 244–245 (2013) 86–93.
- [31] S. Bai, X. Shen, H. Lv, G. Zhu, C. Bao, Y. Shan, Assembly of Ag₃PO₄ nanocrystals on graphene-based nanosheets with enhanced photocatalytic performance, *J. Colloid Interface Sci.*, 405 (2013) 1–9.
- [32] X. Fan, J. Shao, Z. Li, F. Ma, A. Meng, Q. Li, Facile synthesis of rGO/Ag₃PO₄ by enhanced photocatalytic degradation of an organic dye using a microwave-assisted method, *New J. Chem.*, 40 (2016) 1330–1335.
- [33] L. Wang, Y. Zhou, Stable visible light photocatalyst based on the graphene protected Ag₃PO₄ nanocomposite, *Fullerenes Nanotubes Carbon Nanostruct.*, 24 (2016) 588–593.
- [34] W.S. Hummers, R.E. Offeman, Preparation of graphitic oxide, *J. Am. Chem. Soc.*, 80 (1958) 1339.
- [35] D. Chakraborty, S.S. Gupta, Decolourisation of Metanil Yellow by visible-light photocatalysis with N-doped TiO₂ nanoparticles, influence of system parameters and kinetic study, *Desal. Wat. Treat.*, 52 (2014) 5528–5540.
- [36] J. Li, T. Tao, X. Li, J. Zuo, T. Li, J. Lu, S. Li, L. Chen, C. Xi, Y. Liu, Y. Wang, A spectrophotometric method for determination of chemical oxygen demand using home-made reagents, *Desalination*, 239 (2009) 139–145.
- [37] J.F. Shen, B. Yan, M. Shi, H.W. Ma, N. Li, M.X. Ye, One step hydrothermal synthesis of TiO₂-reduced graphene oxide sheets, *J. Mater. Chem.*, 21 (2011) 3415–3421.
- [38] X.F. Yang, H.Y. Cui, Y. Li, J.L. Qin, R.X. Zhang, H. Tang, Fabrication of Ag₃PO₄-graphene composites with highly efficient and stable visible light photocatalytic performance, *ACS Catal.*, 3 (2013) 363–369.
- [39] W.G. Wang, J.G. Yu, Q.J. Xiang, B. Cheng, Enhanced photocatalytic activity of hierarchical macro/mesoporous TiO₂-graphene composites for photodegradation of acetone in air, *Appl. Catal. B*, 119–120 (2012) 109–116.
- [40] Y.H. Ding, P. Zhang, Q. Zhuo, H.M. Ren, Z.M. Yang, Y. Jiang, A green approach to the synthesis of reduced graphene oxide nanosheets under UV irradiation, *Nanotechnology*, 22 (2011) 215601.
- [41] G.L. Huang, Y.F. Zhu, Enhanced photocatalytic activity of ZnWO₄ Catalyst Via Fluorine Doping, *J. Phys. Chem. C*, 111 (2007) 11952–11958.
- [42] P.Y. Dong, Y.H. Wang, B.C. Cao, S.Y. Xin, L.N. Guo, J. Zhang, F.H. Li, Ag₃PO₄/reduced graphite oxide sheets nanocomposites with highly enhanced visible light photocatalytic activity and stability, *Appl. Catal. B*, 132–133 (2013) 45–53.
- [43] Q.H. Liang, Y. Shi, W.J. Ma, Z. Li, X.M. Yang, Enhanced photocatalytic activity and structural stability by hybridizing Ag₃PO₄ nanospheres with graphene oxide sheets, *Phys. Chem. Chem. Phys.*, 14 (2012) 15657–15665.
- [44] Z. Wang, L. Yin, M. Zhang, G.W. Zhou, H. Fei, H.X. Shi, H.J. Dai, Synthesis and characterization of Ag₃PO₄/multiwalled carbon nanotube composite photocatalyst with enhanced photocatalytic activity and stability under visible light, *J. Mater. Sci.*, 49 (2014) 1585–1593.
- [45] H. Wang, Y. Wang, X. Cao, M. Feng, G. Lan, Vibrational properties of graphene and graphene layers, *J. Raman Spectrosc.*, 40 (2009) 1791–1796.
- [46] G.H. Shao, X.J. Zhang, Z.Y. Yuan, Preparation and photocatalytic activity of hierarchically mesoporous-macroporous TiO₂-xNx, *Appl. Catal. B*, 82 (2008) 208–218.
- [47] B.Y. Lee, S.H. Park, S.C. Lee, M. Kang, C.H. Park, S.J. Choung, Optical properties of Pt-TiO₂ catalyst and photocatalytic activities for benzene decomposition, *Kor. J. Chem. Eng.*, 20 (2003) 812–818.
- [48] S.S. Gupta, D. Chakraborty, Photocatalytic decolourisation of toxic dye, Acid Blue 25, with graphene based N-doped titania, *Indian J. Chem.*, 56A (2017) 1293–1301.